

Unsupervised clustering of coral reef bioacoustics

Emma Ozanich, Aaron Thode, Peter Gerstoft
Scripps Institution of Oceanography, UCSD

Lauren A Freeman, Simon Freeman
Naval Underwater Warfare Center Newport
(Dated: October 31, 2021)

An unsupervised process is described for clustering automatic detections in an acoustically active coral reef soundscape. First, acoustic metrics were extracted from spectrograms and timeseries of each detection based on observed properties of signal types and classified using unsupervised clustering methods. Then, deep embedded clustering (DEC) was applied to fixed-length power spectrograms of each detection to learn features and clusters. The clustering methods were compared on simulated bioacoustic signals for fish calls and whale song units with randomly varied signal parameters and additive white noise. Overlap and density of the handpicked features led to reduced accuracy for unsupervised clustering methods. DEC clustering identified clusters with fish calls, whale song, and events with simultaneous fish calls and whale song, but accuracy was reduced when the class sizes were imbalanced. Both clustering approaches were applied to acoustic events detected on directional autonomous seafloor acoustic recorder (DASAR) sensors on a Hawaiian coral reef in February–March 2020. Unsupervised clustering of handpicked features did not distinguish fish calls from whale song. DEC had high recall and correctly classified a majority of whale song. Manual labels indicated a class imbalance between fish calls and whale song at a 3-to-1 ratio, likely leading to reduced DEC clustering accuracy.

I. INTRODUCTION

Machine learning has become commonly used within the acoustics community and the ocean bioacoustics community in particular (Sec VIII in Ref. 3) where automatic detection and classification methods have been under development for marine mammals calls for decades and continue to expand.[2, 7, 15, 31, 32, 34–36, 38] Recently, a smaller set of studies have also considered unsupervised machine learning techniques for analyzing large, unlabelled bioacoustic soundscape data.[10, 11, 20, 39]

Acoustic classification of marine fishes, such as damselfish (family *Pomacentridae*), has been improved through passive acoustic field experiments that have characterized the calls and calling behavior[25, 29, 42] but lacks established terminology across studies and a universally accepted correspondence between calls and behavior.[1] Recently, a few studies have considered automatic classification of fish calls by utilizing machine learning tools. Malfante et al. 2018 extracted time, spectral, and cepstral features for use in supervised classifiers of fish calls in a seagrass meadow. Based on four call types defined by the authors, the machine learning classifiers achieved up to 95% accuracy.[24] Lin et al. 2018 compared the detection performance of a rule-based energy detector to the machine learning methods of periodicity-coded nonnegative matrix factorization and Gaussian mixture models. The machine learning methods were applied to power spectra of croaker calls recorded in shallow water (10–25 m) and then qualitatively compared to the energy detector results.[22] Then, Ibrahim et al. 2018 compared long short-term neural networks (LSTM) and convolutional neural networks (CNN) for supervised classification of grouper croaks in

the time-frequency domain. They found that machine learning outperformed weighted mel-frequency cepstral coefficients, with LSTM achieving over 90% correct classification accuracy on all species tested.[17]

In this paper, the problem of identifying bioacoustic signals in an acoustically active coral reef is addressed using unsupervised machine learning. We consider two approaches for extracting features for clustering:

1. Spectral and time domain features were manually chosen, or handpicked, based on their observed relation to coral reef fish calling and on studies of fish calling spectral and temporal properties.[25, 29, 42]
2. Fixed-length spectrograms were used in a deep embedded clustering (DEC) algorithm,[44] a deep-learning image compression algorithm that ensures accurate image reconstruction from the latent feature vector while encouraging cluster formation among the latent features.[13, 37]

For handpicked features, the statistical properties of different features may vary, and the features are not guaranteed to be separable by unsupervised algorithms. The DEC algorithm aims to address feature separability by jointly learning the features and clusters from the spectrogram. However, DEC on a single-channel spectrogram may have reduced performance when signals overlap or if there are is consistently low signal-to-noise ratio (SNR) within the training data.

Simulated signals were used to compare the limitations of the handpicked feature clustering and DEC. The signals were designed to mimic whale song and fish call pulses recorded on a Hawaiian coral reef, with the SNR and call parameters randomly varied to simulate experimental variation. Accuracy, recall, and precision were

used to measure the classification success of both methods. Then, using transient events detected from an automatic directional detector,[40] both methods were applied to acoustic data recorded in February–March 2020.

In Sec. II, unsupervised clustering theory is overviewed for Gaussian-distributed features with known mean and covariance. A method for visualizing high-dimensional data is also discussed. The handpicked features and their extraction procedure are covered in Sec. IIIA and the DEC theory is reviewed in Sec. IIIB. Section IV details clustering results for simulated coral reef bioacoustic signals: fish calls and whale song units, represented by Gaussian pulses and frequency-modulated (FM) sweeps. Experimental data collection from a Hawaiian coral reef in February 2020 and the directional detection algorithm are outlined in Sec. V. Last, Sec. VI presents the experimental detection and clustering results. Section VII summarizes the approach and discusses challenges associated with the methods and dataset.

II. UNSUPERVISED CLUSTERING

Unsupervised clustering methods are frameworks for categorizing data according to their similarities.[4] The performance of each algorithm depends on the validity of its underlying assumptions for a given feature set. This section discusses the maximum likelihood class boundaries for Gaussian clusters, then describes the K-means and hierarchical agglomerative clustering algorithms.

A. Maximum likelihood of Gaussian clusters

When the generative distribution of the data are known, an exact solution for the optimal clusters can be derived. Assume a P -dimensional vector, $\mathbf{x}_n \in \mathbb{R}^P$, is drawn from one of K Gaussian distributions with mean $\boldsymbol{\mu}_k \in \mathbb{R}^P$ and covariance $\boldsymbol{\Sigma}_k \in \mathbb{R}^{P \times P}$. The analytic solution to the cluster boundaries can be computed using the posterior given by Bayes' theorem,[5]

$$p(C_k|\mathbf{x}) = \frac{p(\mathbf{x}|C_k)p(C_k)}{\sum_j p(\mathbf{x}|C_j)p(C_j)} \quad (1)$$

$$p(\mathbf{x}|C_k) = \frac{1}{(2\pi)^{\frac{P}{2}} |\boldsymbol{\Sigma}_k|^{\frac{1}{2}}} e^{-\frac{1}{2}(\mathbf{x}-\boldsymbol{\mu}_k)^T \boldsymbol{\Sigma}_k^{-1}(\mathbf{x}-\boldsymbol{\mu}_k)}, \quad (2)$$

Where C_k and C_j represent two class labels and each point \mathbf{x}_n belongs to only one class. The optimal boundary between the two classes occurs when the probability of the classes are equal,

$$\begin{aligned} \log p(C_k|\mathbf{x}) &= \log p(C_j|\mathbf{x}) \\ \log p(\mathbf{x}|C_k) + \log C_k &= \log p(\mathbf{x}|C_j) + \log C_j. \end{aligned} \quad (3)$$

Combining (2) and (3) and setting equal to zero:

$$0 = -\frac{1}{2}\mathbf{x}^T(\boldsymbol{\Sigma}_k^{-1} - \boldsymbol{\Sigma}_j^{-1})\mathbf{x} + \mathbf{w}^T \mathbf{x} + \frac{C}{2} \quad (4)$$

$$C = -\boldsymbol{\mu}_k^T \boldsymbol{\Sigma}_k^{-1} \boldsymbol{\mu}_k + \boldsymbol{\mu}_j^T \boldsymbol{\Sigma}_j^{-1} \boldsymbol{\mu}_j - \log \frac{|\boldsymbol{\Sigma}_k|}{|\boldsymbol{\Sigma}_j|} + 2 \log \frac{C_k}{C_j} \quad (5)$$

$$\mathbf{w} = \boldsymbol{\mu}_k \boldsymbol{\Sigma}_k^{-1} - \boldsymbol{\mu}_j \boldsymbol{\Sigma}_j^{-1} \quad (6)$$

The general solution (4) is a P -dimensional parabola, which simplifies to a linear boundary if the distributions have a shared covariance such that $\boldsymbol{\Sigma}_k = \boldsymbol{\Sigma}_j \forall j, k$. In a similar manner, (4) is extensible to $K > 2$ classes.[5]

When $\boldsymbol{\Sigma}_k$ and $\boldsymbol{\mu}_k$ are unknown, the Expectation-Maximization (EM) algorithm can be used to estimate them from a set of data \mathbf{x} , $n = 1, \dots, N$ via the complete data log-likelihood.[33]

This can be solved using an alternating algorithm to update the weighted posterior probability (responsibility) and the class prior, mean, and covariance[33]

$$\text{E step: } r_{nk} = \frac{\pi_k p(\mathbf{x}_n | C_k^{t-1})}{\sum_{k'} \pi_{k'} p(\mathbf{x}_n | C_{k'}^{t-1})} \quad (7)$$

$$\text{M step: } \pi_k = \frac{1}{N} \sum_n r_{nk} \quad (8)$$

$$\boldsymbol{\mu}_k = \frac{\sum_n r_{nk} \mathbf{x}_n}{\sum_n r_{nk}}, \quad \boldsymbol{\Sigma}_k = \frac{\sum_n r_{nk} \mathbf{x}_n \mathbf{x}_n^T}{\sum_n r_{nk}} \quad (9)$$

where C_k^{t-1} represents the k th cluster at step $t-1$.

EM is iterated until both steps converge for K classes. EM requires that the number of clusters, K , be assumed *a priori*, and the estimated covariance matrix can become ill-conditioned if there are fewer than K clusters.

B. K-Means

K-means[16] is an approximation to the EM algorithm that partitions $\mathcal{X} = \{\mathbf{x}_1, \dots, \mathbf{x}_N\}$ into the K clusters. The K-means algorithm requires that K is set by the practitioner and assumes that all clusters are Gaussians with covariance $\boldsymbol{\Sigma} = \sigma^2 \mathbb{I}$ and prior probability $\pi_k = 1/K$, where \mathbb{I} is the identity matrix.

K-means is also called hard EM because it assigns each point to a cluster rather than computing the cluster likelihood. The EM steps are simplified using the K-means assumptions to solve for the optimal clusters,:[5]

$$1. \quad r_{nk} = \begin{cases} 1 & \text{if } k = \arg \min_j \|\mathbf{x}_n - \boldsymbol{\mu}_j\|^2, \\ 0 & \text{otherwise,} \end{cases} \forall n \quad (10)$$

$$2. \quad \boldsymbol{\mu}_k = \frac{1}{|C_k|} \sum_{\mathbf{x}_n \in C_k} \mathbf{x}_n = \frac{\sum_n r_{nk} \mathbf{x}_n}{\sum_n r_{nk}} \quad (11)$$

where C_k is the k th cluster and $|C_k|$ denotes its cardinality or size.

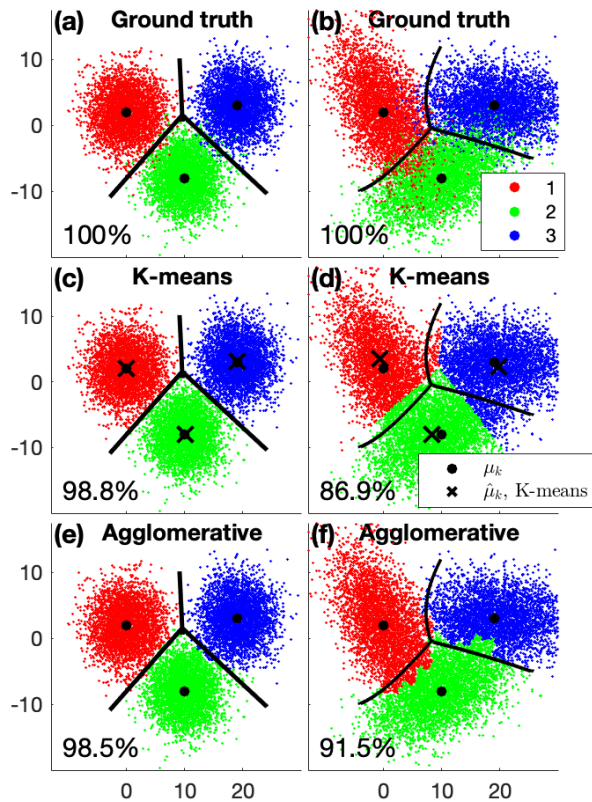


FIG. 1. Clustering on two data distributions using (c,d) K-means and (e,f) agglomerative clustering with Ward’s method, with maximum likelihood boundaries shown by black lines. In the first dataset in (a), the clusters have shared covariances of the form $\sigma^2 \mathbf{I}$ ($\sigma_x^2 = \sigma_y^2 = 3$). The clusters of the second dataset (b) each have different covariances resulting from cluster rotations of $\theta = 120^\circ, 25^\circ$, and 0° counterclockwise ($\sigma_x^2 = 6, \sigma_y^2 = 3$).

K-means will result in the maximum likelihood solution in (4) when the classes are Gaussian with shared covariance, $\Sigma_k = \sigma^2 \mathbf{I} \forall k$. [5] If the true number of classes differs from K , the classes will be incorrectly estimated. In the following, an underlying knowledge of the signal content is assumed for specifying K .

C. Agglomerative hierarchical clustering

Agglomerative hierarchical clustering, [4, 33] also called bottom-up clustering, partitions a set of N data points, $\mathcal{X} = \{\mathbf{x}_1, \dots, \mathbf{x}_N\}$, into K clusters by grouping the most similar data at each step. Hierarchical clustering successively merges nearby clusters until the stop criterion is achieved. In this case, the stop criterion is met when K or fewer classes remain, where K must be set by the practitioner.

Agglomerative methods preferentially cluster dense points, improving robustness to outliers. The tradeoff is decreased performance when clusters are dense and

close. A related bottom-up approach has been demonstrated to work well for clustering dolphin echolocation clicks. [10, 11]

To initialize from bottom-up, each point begins as its own cluster, $C_{k_0} = \mathbf{x}_n, k_0 = 1, \dots, N$. Then, clusters that satisfy the minimum distance requirement are merged

$$j, k = \arg \min_{i, i'} d(i, i') \quad (12)$$

$$C_{k_1} = \{C_j \cup C_k\}, \quad (13)$$

where $d(i, i')$ is the distance between clusters i and i' . The agglomerative process is repeated M times, until there are at most K clusters remaining with $C_{k_M}, k_M = 1, \dots, K$.

The distance metric chosen here is *Ward’s method*. [18] Ward’s method measures the within-cluster variance of two merged clusters. The variance introduced by merging two sub-clusters, C_1 and C_2 with means μ_1 and μ_2 , is measured by the increase in the incremental sum-of-squares, [30]

$$\begin{aligned} d(C_1, C_2) &= \sum_{i \in (C_1 \cup C_2)} (\mathbf{x}_i - (\mu_1 + \mu_2))^2 - \sum_{j \in C_1} (\mathbf{x}_j - \mu_1)^2 - \sum_{k \in C_2} (\mathbf{x}_k - \mu_2)^2 \\ &= (|C_1| + |C_2|)(\mu_1 + \mu_2)^2 - |C_1| \mu_1^2 - |C_2| \mu_2^2 \\ &= \frac{2|C_1||C_2|}{|C_1| + |C_2|} \|\mu_1 - \mu_2\|_2^2. \end{aligned} \quad (14)$$

where $\mu_1 = \frac{1}{|C_1|} \sum_{j \in C_1} \mathbf{x}_j$ and $\mu_2 = \frac{1}{|C_2|} \sum_{k \in C_2} \mathbf{x}_k$. $|C_1|$ and $|C_2|$ are the cardinality of cluster C_1 and C_2 . In practice, \sqrt{d} from (14) was used.

If the number of true classes differs from K , the final output may be misinterpreted. However, the hierarchical agglomerative clustering cost function is agnostic of K , and the history of clusters can be retrieved to improve understanding of the feature similarities.

D. Clustering simulations

Three 2D Gaussian distributions, each with $N = 6,666$ points, were used to simulate overlapping clusters (Fig. 1). The true cluster means were $\mu_1 = (0, 2)$, $\mu_2 = (10, -8)$, and $\mu_3 = (21, 3)$. The covariance of the first dataset was

$$\Sigma_{C_1} = \begin{bmatrix} \sigma_x^2 & 0 \\ 0 & \sigma_y^2 \end{bmatrix} \quad (15)$$

with $\sigma_x^2 = \sigma_y^2 = 3$. For the first dataset (Fig. 1a), there were no off-diagonal covariance terms.

The second dataset (Fig. 1b) was generated by rotating the data counterclockwise at θ , with

$$\Sigma_{C_2} = \begin{bmatrix} \cos(\theta) & -\sin(\theta) \\ \sin(\theta) & \cos(\theta) \end{bmatrix} \begin{bmatrix} \sigma_x^2 & 0 \\ 0 & \sigma_y^2 \end{bmatrix} \begin{bmatrix} \cos(\theta) & -\sin(\theta) \\ \sin(\theta) & \cos(\theta) \end{bmatrix}^T \quad (16)$$

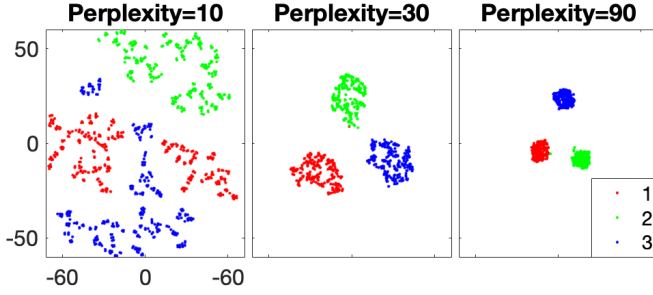


FIG. 2. Varying values of perplexity for t-SNE on $N=1000$ randomly drawn points $\mathbf{x}_n \in \mathbb{R}^3$, $n = 1, \dots, N$. The default perplexity value was 30.

with $\sigma_x^2 = 6$, $\sigma_y^2 = 3$. The three clusters were rotated by $\theta = 120^\circ, 25^\circ$, and 0° . Off-diagonal covariance terms were introduced by the rotation. In realistic data, a strongly rotated cluster such as Class 1 may represent two highly correlated features.

The K-means algorithm assumes that clusters are spatially distributed around a mean with diagonal covariance. Thus, K-means performs best for the first dataset with identical, diagonal covariance for all clusters. By incorporating intercluster distance, the Ward metric is also able to identify 3 classes but is susceptible to misclassifying data where dense clusters overlap. When the cluster covariances are not of the form $\sigma^2\mathbb{I}$, K-means is no longer a valid approximation to the maximum likelihood solution.

E. Visualization of high-dimensional data

For data with more than two dimensions, $\mathbf{x}_n \in \mathbb{R}^P$ for $P > 2$, clusters may be visualized by applying dimensionality reduction. In this study, 2D t-Stochastic Neighbor Embedding (t-SNE)[14] was used to visualize P -dimensional features.

The similarity of one point, $\mathbf{x}_i \in \mathbb{R}^P$, to another point, $\mathbf{x}_j \in \mathbb{R}^P$, is found by computing the conditional probability that the points will be neighbors within a Gaussian density centered at \mathbf{x}_i , [14]

$$p_{j|i} = \frac{e^{-\frac{1}{2\sigma_i^2}\|\mathbf{x}_i - \mathbf{x}_j\|^2}}{\sum_{k \neq l} e^{-\frac{1}{2\sigma_i^2}\|\mathbf{x}_k - \mathbf{x}_l\|^2}}, \quad p_{i|i} = 0 \quad (17)$$

where $i, j=1, \dots, N$. The neighborhood of \mathbf{x}_i , as determined by σ_i , $i=1, \dots, N$ is defined implicitly in terms of the perplexity (Fig. 2), [14, 23]

$$\text{perplexity}(P_i) = 2^{H(P_i)} \quad (18)$$

$$H(P_i) = - \sum_{j=1}^N p_{j|i} \log_2 p_{j|i} \quad (19)$$

where $P_i = \sum_j p_{j|i}$, and H is the Shannon entropy. The optimal value of σ_i in (17) for each point is solved with a binary search for a given value of perplexity. [23]

Then, a set of two-dimensional point projections is randomly initialized with zero-mean Gaussians of low variance, [14] $\mathbf{y}_i \in \mathcal{N}(\mathbf{0}, 10^{-4}\mathbf{I})$. The optimal point projections are found by minimizing the Kullback-Leibler (KL) divergence between the original distribution and the Student's t-distribution of the proposed data,

$$q_{j|i} = \frac{(1 + \|\mathbf{y}_i - \mathbf{y}_j\|^2)^{-1}}{\sum_{k \neq l} (1 + \|\mathbf{y}_k - \mathbf{y}_l\|^2)^{-1}}, \quad q_{i|i} = 0 \quad (20)$$

$$KL(P||Q) = - \sum_{i \neq j} \sum_{j=1}^N p_{j|i} \log \frac{p_{j|i}}{q_{j|i}}. \quad (21)$$

In contrast to classic SNE which uses only Gaussians, t-SNE's use of the Student t-distribution further penalizes outliers. [14]

As shown in Fig. 2, the value of perplexity should be varied according to user preference to obtain the desired visualization. Although the default perplexity value in the MATLAB implementation [23] is 30, larger datasets require higher perplexity.

III. FEATURE EXTRACTION

Feature extraction may be considered the most important step for unsupervised clustering, as the feature properties determine cluster performance. Here, we examine two feature extraction approaches: handpicked features and deep embedded clustering. The handpicked feature vectors were stacked to form a feature matrix to be used with unsupervised clustering methods. Deep embedded clustering jointly learns and clusters feature vectors using a convolutional autoencoder neural network. [44]

A. Handpicked features

The handpicked features (Table I, Fig. 3) are time-frequency properties known to relate to fish call type including power, duration, and peak frequency [25, 29, 42] as well as timeseries estimates of impulsive noise. [24, 28] The spectrogram parameters were 256-point FFT with 90% overlap, $dt=0.0256$ s, and $df=3.9$ Hz.

If t_1 and t_2 represent the absolute start and end times for a detected event, the event duration is

$$\text{Duration(s)} = \Delta t = t_2 - t_1. \quad (22)$$

Between t_1 and t_2 , the event power spectrogram $|\mathbf{S}|^2 \in \mathbb{R}^{N_f \times N_t}$ was computed. Across the power spectrogram, the median power and peak frequency were extracted

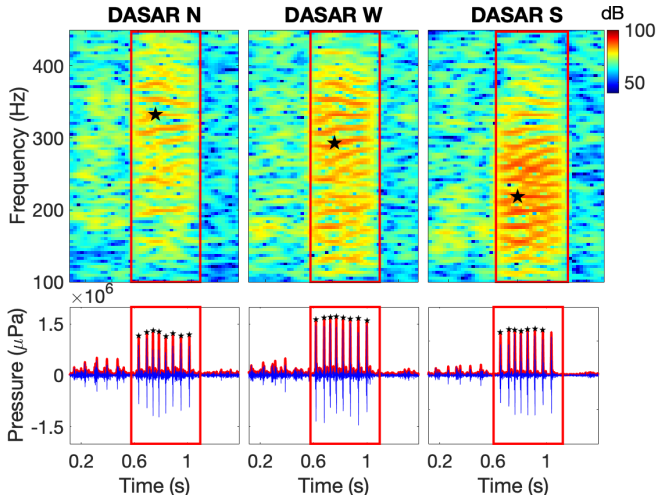


FIG. 3. Handpicked features of a fish call event on February 25, 07:12 HST, measured on directional autonomous seafloor acoustic recordings (DASARs) N, W, and S. A call duration of 0.52 s was determined during the detection process. The spectrograms (a–c) were used to extract peak frequencies (black star) from 219–332 Hz and median PSD from 72.8–76.3 dB. The timeseries envelope (d–f) was used to extract the kurtosis values of 18–21, cross-sensor coherences of 0.72–0.74, and 8 temporal peaks. DASAR S was the closest to the call.

TABLE I. Event features estimated for automatically detected pulse sounds.

Feature Name (units)	Description
Kurtosis	Fourth moment normalized by the squared variance
Npeaks (count)	Number of peaks with at least 5 dB prominence <i>re</i> the standard deviation
Peak frequency (Hz)	Frequency of the peak power spectral density
<i>Features for experimental data only</i>	
Duration (s)	Length of detected event
Coherence	Normalized time coherence between DASARs
Median PSD (dB)	Median power spectral density (PSD) across event mask

(Fig. 3a–c), with

$$\text{Median PSD} = \text{median}_{i,j} S^{(i,j)}$$

$$\text{Peak freq.} = \arg \max_i \left(\max_j S^{(i,j)} \right), \\ i = 1, \dots, N_f, \quad j = 1, \dots, N_t.$$

In simulation, the duration was fixed and the signal-to-noise ratio was randomized. Neither feature was used for clustering.

The pressure timeseries $\mathbf{y} \in \mathbb{R}^N$ was extracted between

t_1 and t_2 (Fig. 3). For the experimental data, the vector sensor x- and y- velocity channels, \mathbf{v}_x and \mathbf{v}_y , were used to create a beamformed pressure timeseries, $\mathbf{y}_b \in \mathbb{R}^N$, for improved detection SNR,

$$\mathbf{y}_b = \mathbf{y} + Z_0 \left[\mathbf{v}_x \sin(\hat{\theta}) + \mathbf{v}_y \cos(\hat{\theta}) \right], \quad (23)$$

where $Z_0 = \rho c$ is the impedance in water with density ρ ($kg \cdot m^3$) and sound speed c ($m \cdot s^{-1}$), a scaling term to ensure all terms were in pressure units of $kg \cdot m^{-1} s^{-2}$ ($N \cdot m^{-2}$). [41] $\hat{\theta}$ is the estimated azimuth of the detected signal. For the simulated data, $\mathbf{v}_x = \mathbf{v}_y = \mathbf{0}$ and $\mathbf{y}_b \equiv \mathbf{y}$.

Three metrics were chosen for timeseries extraction: kurtosis, number of peaks, and cross-sensor coherence. The kurtosis is a ratio of moments and has recently been applied to the task of differentiating impulsive from non-impulsive sounds, [24, 28]

$$\text{Kurtosis} = \frac{\mu_4}{\sigma^2}, \quad \mu_4 = \frac{1}{N} \sum_{i=1}^N [y_b[i] - \bar{y}_b]^4 \quad (24)$$

σ^2 is the variance and \bar{y}_b is the arithmetic mean.

The number of peaks and cross-sensor coherence were extracted from the Hilbert transform of the beamformed pressure timeseries (Fig. 3)

$$\tilde{\mathbf{y}}_b = \mathcal{H}(\mathbf{y}_b)$$

where $\mathcal{H}()$ is the Hilbert transform. The number of peaks in the timeseries may be an indicator of fish species and call context for Hawaiian reef fish. [29, 42] Here, the number of peaks was defined as the number of local maxima with at least 5dB prominence relative to the standard deviation,

$$\text{Npeaks} = \sum_{j \in (a,b)} \mathbb{I}(\max_j \tilde{y}_b[j] > C + \max \min_j \tilde{y}_b[j]), \quad (25)$$

$$C = \sigma \cdot 10^{1/2}$$

where (a, b) is an interval in $\tilde{\mathbf{y}}_b$, σ is the standard deviation, and $\mathbb{I}(x) = 1$ if $x = \text{True}$, 0 if $x = \text{False}$.

Last, for the experimental detections, the normalized correlation coefficient of the timeseries envelope across DASARs was computed to measure the spatial coherence of the signal propagation,

$$\text{Coherence} = \max_i \frac{1}{C} \sum_{m=i}^{N-1} \tilde{y}_{b,N}[m] \tilde{y}_{b,S}[m-i] \quad (26)$$

$$C = \sqrt{\|\tilde{\mathbf{y}}_{b,N}\|_2^2 + \|\tilde{\mathbf{y}}_{b,S}\|_2^2},$$

where $N-1$ is the number of samples per event, which varies for each detection. $\tilde{\mathbf{y}}_{b,N}$ and $\tilde{\mathbf{y}}_{b,S}$ represent the timeseries extracted on the North and South DASARs.

B. Deep embedded clustering

Deep embedded clustering (DEC) is a modified convolutional autoencoder, a neural network-based feature

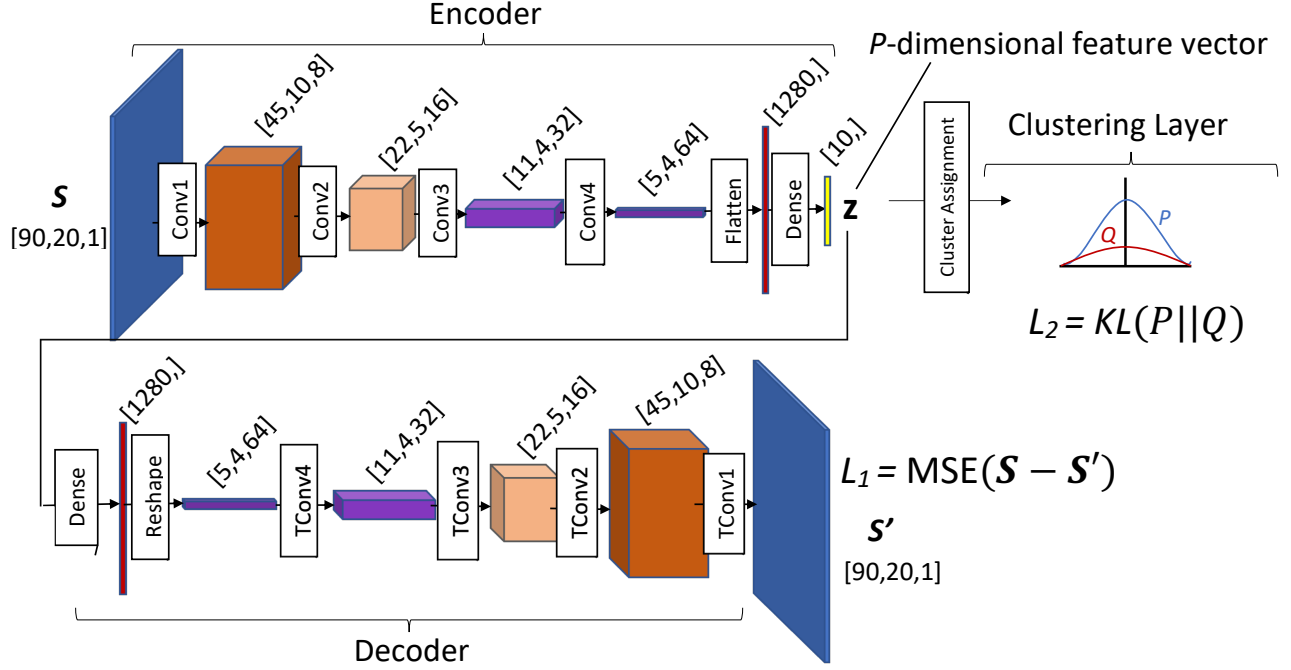


FIG. 4. Architecture of the deep embedded encoding (DEC) convolutional model. Convolutional filters were sized 3x3 and used the rectified linear unit (ReLU) activation function.

learning method,[12] that encourages separability of its learned feature space (Fig. 4). The structure consists of two stacked networks: the encoder network, which maps input data into a lower-dimensional or latent space, and the decoder network, which reconstructs an approximation of the input from the latent space. Here, the architecture was compressive, with the input image down-sampled by the network with 2D convolutions of stride length 2. The Rectified Linear Unit (ReLU) was used to transform the outputs at each layer,

$$f(x) = \begin{cases} 1 & x \geq 0 \\ 0 & x < 0. \end{cases} \quad (27)$$

The use of this model for clustering of bioacoustic coral reef signals was inspired by its recent application to unlabeled seismic events.[37] Additional details of the model are given in Fig. 4 and Table II. In this study, the input images are the same as the output labels to encourage accurate image reconstruction.

The latent feature separation is accomplished by incorporating two loss functions at different stages of training: mean squared reconstruction error (MSE) between the input and output spectrogram, and Kullback-Leibler

divergence,[13, 44]

$$KL(P||Q) = \sum_n \sum_k p_{nk} \log \left(\frac{p_{nk}}{q_{nk}} \right) \quad (28)$$

$$q_{nk} = \frac{(1 + \|\mathbf{z}_n - \boldsymbol{\mu}_k\|^2)^{-1}}{\sum_j (1 + \|\mathbf{z}_n - \boldsymbol{\mu}_j\|^2)^{-1}} \quad (29)$$

$$p_{nk} = \frac{q_{nk}^2 / \sum_m q_{mk}}{\sum_j (q_{nj}^2 / \sum_m q_{mk})}, \quad (30)$$

where $\mathbf{z}_n \in \mathbb{R}^P$ is the latent feature vector of the n th spectrogram input and $\boldsymbol{\mu}_k$ is the k th cluster mean. (29) is the empirically estimated Student's t-distribution and (30) further penalizes points that are distant from a cluster center.[13]

Unlike supervised machine learning, training labels are not available in unsupervised learning and DEC. Instead, the DEC was trained with fixed-length spectrogram images $\log_{10} |\mathbf{S}_n|^2 \in \mathbb{R}^{N_f \times N_t}$ of 0.5 s = $N_t \cdot dT$ at its input and output, where events longer than 0.5 s were clipped to length. This feature-learning approach is analogous to principal component analysis.

First, the DEC (Fig. 4) was pretrained to learn latent features using mean squared reconstruction error loss for 1000 epochs with the Adam optimizer[19] and learning rate of 10^{-3} . The pretrained latent features \mathbf{z}_n were then clustered with K-means to initialize the deep clustering, with means $\boldsymbol{\mu}_k$, $k = 1, \dots, K$. The DEC was trained for an additional 20 epochs using the joint clus-

TABLE II. Network architecture used in deep embedded clustering. The input and output shapes are given as [height, width, depth]. The kernel size is the shape of the two dimensional convolutional filters in [height, width].

Layer Name	Layer Type	Input shape	Filters	Kernel size	Stride	Activation	Output shape	Parameters
Conv1	2D Convolution	[90,20,1]	8	[3,3]	[2,2]	ReLU	[45,10,8]	80
	2D Conv.	[45,10,8]	8	[2,1]	[1,1]	ReLU	[44,10,8]	136
Conv2	2D Conv.	[44,10,8]	16	[3,3]	[2,2]	ReLU	[22,5,16]	1168
	2D Conv.	[22,5,16]	16	[1,2]	[1,1]	ReLU	[22,4,16]	528
Conv3	2D Conv.	[22,4,16]	32	[2,1]	[2,1]	ReLU	[11,4,32]	1056
	2D Conv.	[11,4,32]	64	[2,1]	[1,1]	ReLU	[10,4,64]	4160
Conv4	2D Conv.	[10,4,64]	64	[2,1]	[2,1]	ReLU	[5,4,64]	8256
Flatten	Flatten	[5,4,64]	-	-	-	-	[1280]	0
Encoded	Fully Connected	[1280]	-	-	-	ReLU	[10]	6405
Dense	Fully Connected	[15]	-	-	-	ReLU	[1280]	7680
Reshape		[1280]	-	-	-	-	[5,4,64]	0
TConv4	Transposed Convolution	[5,4,64]	32	[2,1]	[2,1]	ReLU	[10,4,32]	4128
	T. Conv.	[10,4,32]	32	[2,1]	[1,1]	ReLU	[11,4,32]	2080
TConv3	T. Conv.	[11,4,32]	16	[2,1]	[2,1]	ReLU	[22,4,16]	1040
	T. Conv.	[22,4,16]	16	[1,2]	[1,1]	ReLU	[22,5,16]	528
TConv2	T. Conv.	[22,5,16]	8	[3,3]	[2,2]	ReLU	[44,10,8]	1160
	T. Conv.	[44,10,8]	8	[2,1]	[1,1]	ReLU	[45,10,8]	136
TConv1	T. Conv.	[45,10,8]	1	[3,3]	[2,2]	Linear	[90,20,1]	73

tering/reconstruction loss function,

$$L = 0.1 \cdot KL + 0.9 \cdot MSE, \quad (31)$$

with KL from (28).

The DEC was written in Keras[6] using Tensorflow[9].

C. Feature matrix

An $N \times P$ feature matrix was constructed by concatenating the feature vectors for each event,

$$\mathbf{Z} = [\mathbf{z}_1, \dots, \mathbf{z}_N]^T \in \mathbb{R}^{N \times P}, \quad (32)$$

with $\mathbf{z}_n \in \mathbb{R}^P$ ($N \gg P$). The feature vectors \mathbf{z}_n were automatically extracted handpicked features, with $P = 6$ (Sec. IIIa). The clustering algorithms in Sec. II were used to find K P -dimensional cluster means. All N points were assigned to a unique cluster.

IV. SIMULATIONS

A set of coral reef bioacoustic events was simulated to compare handpicked features and deep embedded clustering under varying conditions. A total of 10,000 events were simulated to mimic recorded whale song and fish pulses or pulse trains (Fig. 5). The signals were simulated as timeseries sampled at 1kHz, preprocessed as spectrogram images using a 256-pt FFT with 90% overlap, and then clipped to 0.5 s.

The DEC latent feature dimension was optimized over a range of values. The optimal DEC performance was

TABLE III. Signal parameters were drawn from random distributions for each simulated event.

	FM Sweep	Pulse train
Duration/Width (s)	$T \in \mathcal{U}(0.2, 0.4)$	$\tau = 0.005$
Delay (s)	$t_0 \in \mathcal{U}(-0.1, 0.1)$	$t_0 \in \mathcal{U}(-0.1, 0.1)$
Frequency (Hz)	$f_0 \in \mathcal{U}(100, 400)$	$f_c = 200$
	$\Delta f \in \mathcal{U}(-150, 150)$	
Peak spacing (s)		$\Delta t \in 0.47 * \text{beta}(4, 23)$
Number of peaks		$N \in [13 * \text{beta}(3.5, 8)]$
SNR (dB)	$SNR \in \mathcal{U}(15, 30)$	$SNR \in \mathcal{U}(0, 30)$

compared to unsupervised clustering with automatically extracted handpicked features. Then, a third class containing an overlapping fish call and whale song was included, with 33% of the total samples belonging to each class.

Quadratic FM sweeps mimic parts of humpback whale song. The equation for the instantaneous frequency of a quadratic sweep is[26]

$$f(t) = \beta t^2 + 2\pi f_0, \quad \beta = \frac{2\pi \Delta f}{T} \quad (33)$$

where f_0 is the initial frequency, Δf is the total bandwidth, and T is the duration of the signal. The signal is an FM upsweep when $\beta > 0$, an FM downsweep when $\beta < 0$ and a tonal when $\beta = 0$. The phase of the time domain signal can be found by integrating the instantana-

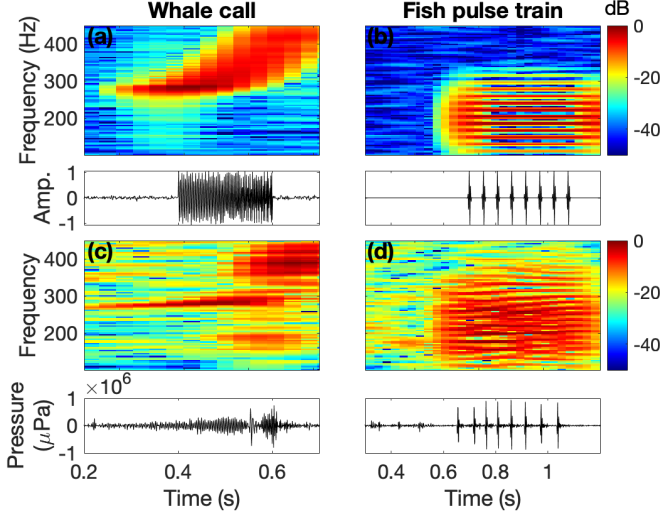


FIG. 5. Simulated (a–b) and measured (c–d) coral reef bioacoustic signals before clipping. Whale calls were simulated with an FM upsweep (a,c), and fish pulse trains were simulated with superimposed Gaussian pulses (b,d). White noise was added to both signals at 25 dB SNR relative to the mean signal power.

neous frequency[26]

$$\Phi(t) = \int_0^{t-t_0} (\beta t^2 + 2\pi f_0) dt \quad (34)$$

$$y(t) = \sin(\Phi(t)) = \sin\left(\frac{\beta}{3}(t-t_0)^3 + 2\pi f_0(t-t_0)\right), \quad (35)$$

where t_0 is the time delay of the signal start.

Timeseries of impulses, or pulse trains, were used to simulate fish calls. The pulses were a set of N superimposed Gaussian-modulated sinusoids[43] spaced Δt apart

$$y(t) = \sum_{i=0}^{N-1} e^{-a|t-i\Delta t-t_0|^2} \sin(2\pi f_c(t-i\Delta t-t_0)) \quad (36)$$

$$a = \tau^{-2} 2 \log(2),$$

where τ is the half-power pulse width and f_c is the center frequency.

The signal parameters were varied randomly for each sample (Table III). Pulse width and center frequency were fixed to achieve a representative pulse structure. The number of pulses and spacing were drawn from experimentally estimated distributions. The duration, initial frequency, and total bandwidth of the FM sweep were drawn at uniform random from a range of realistically observed values. All signals were centered within the 0.5 s spectrogram and assigned a random delay of within ± 0.1 s.

White noise was added to the simulated signals using

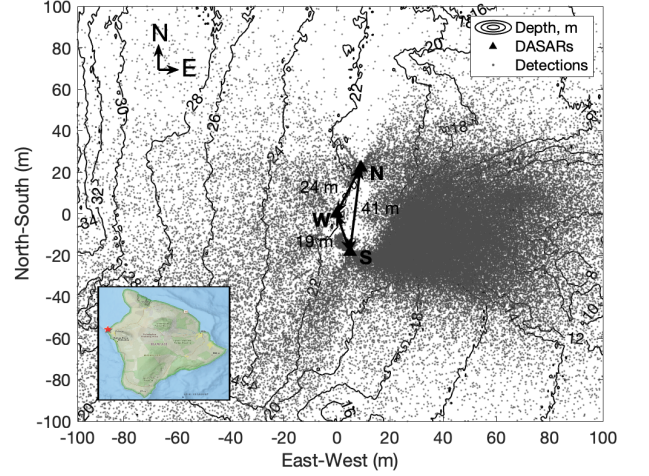


FIG. 6. Diagram of the DASAR array deployed adjacent to a coral reef on the island of Hawaii.[8] The estimated detection locations are shown as gray dots. The majority of the reef is located due east of the array. The sensor positions were measured on the seafloor relative to DASAR W.

a fixed signal-to-noise ratio (SNR),

$$SNR = 10 \log_{10} \frac{\sigma_s^2}{\sigma_n^2}, \quad \sigma_n^2 = \sigma_s^2 10^{-SNR/10}, \quad (37)$$

$$y(t) = y(t) + \mathcal{N}(0, \sigma_n^2 \mathbb{I}), \quad (38)$$

where σ_s^2 is the signal power and σ_n^2 is the noise power. The SNR range of each signal was determined from the experimental spectrograms during manual labeling. The SNR was estimated as the difference of the peak signal power to the median power of the background.

The signal power was estimated as the bandwidth-normalized mean power over the signal duration,[27]

$$\sigma_{s,FM}^2 = \frac{1}{\Delta f \cdot T} \int_{t_0}^{t_0+T} |y(t)|^2 dt, \quad (39)$$

$$\sigma_{s,pulse}^2 = \frac{1}{\Delta f \cdot 4\tau} \int_{t_0-2\tau}^{t_0+2\tau} |y(t)|^2 dt. \quad (40)$$

Following Sec. IIIA, three handpicked features were extracted: peak frequency (23), kurtosis (24), and number of timeseries peaks (25). Duration, median power, and cross-sensor coherence were excluded due to limitations of the fixed simulation parameters. Then, K-means and hierarchical clustering were applied to the feature matrix to discover $K = 2$ classes (fish or whale) or $K = 3$ (fish, whale, or both).

Deep embedded clustering was applied directly to the spectrogram images according to Sec. IIIB.

V. DATA COLLECTION AND PROCESSING

Three directional autonomous seafloor acoustic recorders (DASARs) were deployed adjacent to a coral

reef westward of the island of Hawaii. The DASARs, labeled N, W, and S from north to south, measured pressure and lateral particle velocity with x - and y -components oriented at orthogonal compass directions. The array was roughly oriented N-S with inter-sensor spacing about 15 m (Fig. 6).

The DASARs recorded continuously for 7 days with a sampling rate of 1 kHz. This study considers a 24-hour period on February 25, 2020. During this period, the dominant soundscape contributors below 500 Hz were reef fish, humpback whales, and motor noise from transiting surface boats, with boat noise occurring predominantly during daylight hours and fish calling most pronounced during the dusk hours.

The data were processed in 5 minute chunks to account for DASAR clock drift. First, a 256-point FFT with 90% overlap and Hanning window was used to generate the complex pressure spectrogram, matrix $\mathbf{S} \in \mathbb{C}^{N_f \times N_t}$ with units $\mu\text{Pa}\cdot\text{Hz}^{-1}$, with $dt = 0.026$ s and $df = 3.91$ Hz. The complex spectrograms of the x - and y -particle velocity, matrices $\mathbf{V}_x \in \mathbb{C}^{N_f \times N_t}$ and $\mathbf{V}_y \in \mathbb{C}^{N_f \times N_t}$, were generated identically to \mathbf{S} with units $m\cdot s^{-1}$. Then, the spectrograms from two sensors were cross-correlated along time to find the relative clock delay, assumed constant across 5 minutes.

The active intensity, a measure of in-plane energy, was used to determine the noise directionality:

$$\mathbf{A} = \text{atan2}(\Re\{\mathbf{S} \odot \mathbf{V}_y^*\}, \Re\{\mathbf{S} \odot \mathbf{V}_x^*\}), \quad (41)$$

* is the complex conjugate and \Re the real component. Atan2 is an elementwise operation with domain $(0^\circ, 359^\circ)$, defined counterclockwise from the y -axis ($0^\circ = \text{North}$), where for each (x, y) ,

$$\text{atan2}(y, x) = \begin{cases} \arctan\left(\frac{x}{y}\right) & y > 0 \\ 180^\circ + \arctan\left(\frac{x}{y}\right) & y < 0. \end{cases} \quad (42)$$

\mathbf{A} is therefore the time-frequency representation of compass directionality. In the following, matrix \mathbf{A}_N is called the *azigram* for DASAR N, likewise for \mathbf{A}_W and \mathbf{A}_S .

A. Event detection

A directional event detector,[40] was developed to utilize the DASARs' directional capability by combining two DASARs, based on the assumptions:

1. An event arrives from a constant azimuthal sector for each DASAR.
2. Target events are broadband below 500 Hz. The minimum required bandwidth was set with an empirical threshold.

The detection algorithm is demonstrated in Fig. 7. First, the azigrams for the north- and southmost DASARs, \mathbf{A}_N

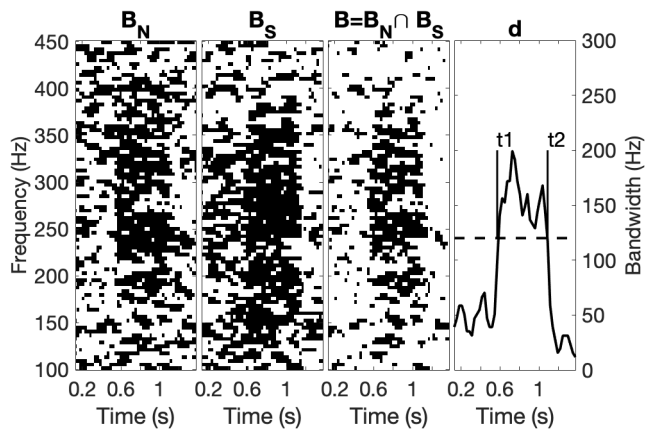


FIG. 7. Directional detector for a fish call event on February 25, 07:12 HST, with DASAR N looking between 135° – 225° and DASAR S looking between 45° – 135° (clockwise from north). The overlap of the binary masks, summed across frequency, defines the detection timeseries.

and \mathbf{A}_S , were used to create binary maps \mathbf{B}_N and \mathbf{B}_S of time-frequency points within a fixed azimuthal sector,

$$\mathbf{B}_N = \mathbb{I}(\theta_N^{(1)} < \mathbf{A}_N \leq \theta_N^{(2)}), \quad (43)$$

and likewise for \mathbf{B}_S (Fig. 7a,b). \mathbb{I} is the elementwise identity function, with $\mathbb{I}(\text{true}) = \mathbf{1}$. Binary maps were generated for all combinations of azimuthal sectors θ_N , $\theta_S \in ([0^\circ, \Delta\theta^\circ]^T, [\frac{\Delta\theta^\circ}{2}, \frac{3\Delta\theta^\circ}{2}]^T, \dots, [(360-\Delta\theta)^\circ, 360^\circ])$.

Next, overlapping signals on both DASARs were discovered by creating a combined map (Fig. 7c),

$$\mathbf{B} = \mathbf{B}_N \cap \mathbf{B}_S. \quad (44)$$

The detection timeseries was generated by summing across frequency of events,

$$\mathbf{d} = df * \sum_i \mathbf{B}(i, :) \quad (45)$$

\mathbf{d} measures the bandwidth of an event. Event start and end times were determined for $d_j > T$, $j = 1, \dots, N_t$ for threshold T . Events separated by less than $M_{\text{sep}} \cdot dt$ were merged and events longer than T_{max} were removed.

For this study, the detector parameters were $\Delta\theta = 90^\circ$, $T = 120$ Hz, $M_{\text{sep}} = 1$ ($M_{\text{sep}} \cdot dt = 0.0256$ s), and $T_{\text{max}} = 2$ s. Detected events were localized[21] to ensure physicality and that their signal had sufficient bandwidth for feature extraction.

Detections for which the localization algorithm failed to converge were discarded. The remaining events were spatially filtered within a 100 m by 100 m box from DASAR S (Fig. 6). 92,736 localizable detections within 100 m were kept for further analysis, on average about 1 detection per second.

Fig. 8 shows the number of events detected along with extracted feature median, 10%, and 90% levels for every

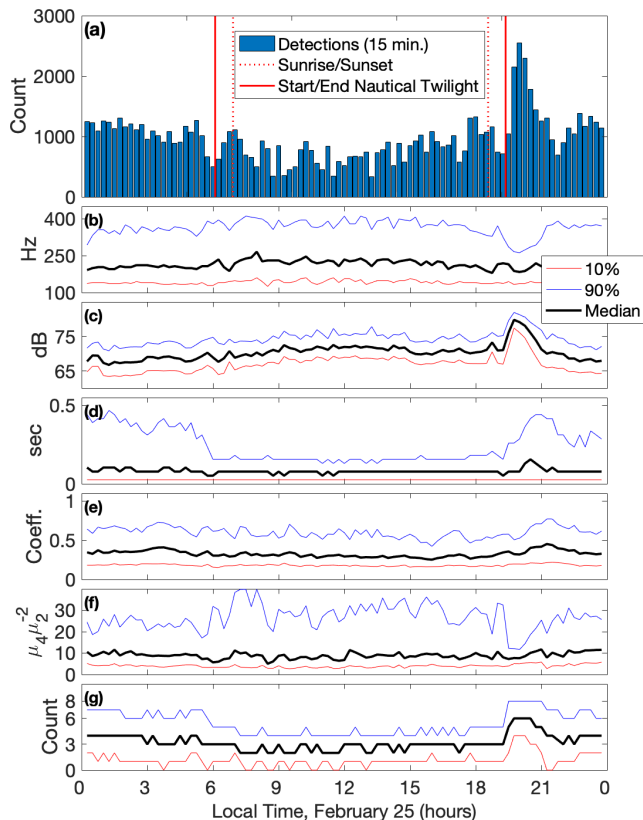


FIG. 8. (a) Number of detected events per 15 minutes on February 25 and (b–g) 10%, 50%, and 90% levels per 15 minutes for each feature: (b) peak frequency, (c) median time-frequency power, (d) event duration, (e) normalized time coherence between sensors, (f) kurtosis, and (g) number of time peaks. All features were measured on the DASAR S. The coherence is the normalized correlation lag coefficient between DASARs N and S.

15 minutes. Fish calls were most common during nighttime, with pulse trains peaking during the evening chorus after nautical twilight (19:15 HST). The evening chorus corresponded to a visible increase in median power, event duration, and number of time peaks and a visible decrease in the 90th percentiles of peak frequency and kurtosis.

VI. CLUSTERING ANALYSIS

A. Metrics

The performance of the handpicked feature clustering and DEC was measured by their accuracy, precision, and

recall,

$$\text{Accuracy} = \frac{1}{N} \sum_{i=1}^N \mathbb{I}(t_i, \hat{t}_i), \quad t_i, \hat{t}_i \in \{0, 1, 2\} \quad (46)$$

$$\text{Precision} = \frac{\sum_{i=1}^N \mathbb{I}(t_i, \hat{t}_i)}{\sum_{j=1}^N \mathbb{I}(\hat{t}_j, 0)}, \quad \text{Recall} = \frac{\sum_{i=1}^N \mathbb{I}(t_i, \hat{t}_i)}{\sum_{j=1}^N \mathbb{I}(t_j, 0)} \quad (47)$$

where t_i is the true label and \hat{t}_i is the class prediction. Here, whale song (label 0) was the true class. Precision (positive predictive value or PPV) measured the ratio of correctly predicted whale song events to total predicted whale song. Recall (hit rate or true positive rate) measured the ratio of correctly classified whale song events to the true total. Higher metrics correspond to improved performance, with perfect performance given by accuracy, precision, and recall all equal to 1.

B. Simulations

First, the handpicked features were examined for separability for $K = 2$ equal-sized classes (fish, whale) and $K = 3$ classes (fish, whale, both) (Fig. 9). Whale song and fish call overlapped in peak frequency and in the number of automatically extracted temporal peaks. The signals were most strongly separated by kurtosis, with whale song having very low kurtosis. The optimal clustering was found when all features were included. The handpicked features were clustered using the unsupervised clustering methods K-means and hierarchical agglomerative clustering (Table IV), with $K = 2$ and $K = 3$ assumed for each case. The known simulation labels were used for post-clustering comparison of the methods.

For 2 equal-sized classes, K-means had marginally higher accuracy and recall than hierarchical clustering, but lower precision (Table IV), indicating that the signal clusters were not equidistant in feature space. For $K = 2$ with imbalanced classes, only 25% of simulated events were whale song, with the remaining 75% fish calls (2500/7500). In this case, hierarchical agglomerative clustering had slightly higher accuracy and recall, but slightly lower precision than K-means. The accuracy, recall, and precision were overall higher for the imbalanced classes (Table IV), which is likely reflective of an imbalance in feature densities for the different classes.

The classification accuracy for 3 equal-sized classes was higher than for 2 equal-sized classes due to the choice of simulation SNR, which was selected as the higher of the two signals (15–30 dB) for the combined features. The handpicked feature values for the combined fish and whale class were between those of whale song or fish call alone. Overall, low recall and accuracy values for the handpicked feature clustering indicate that many of the whale song events were misclassified, but high precision indicates that most events classified as whale song were correct.

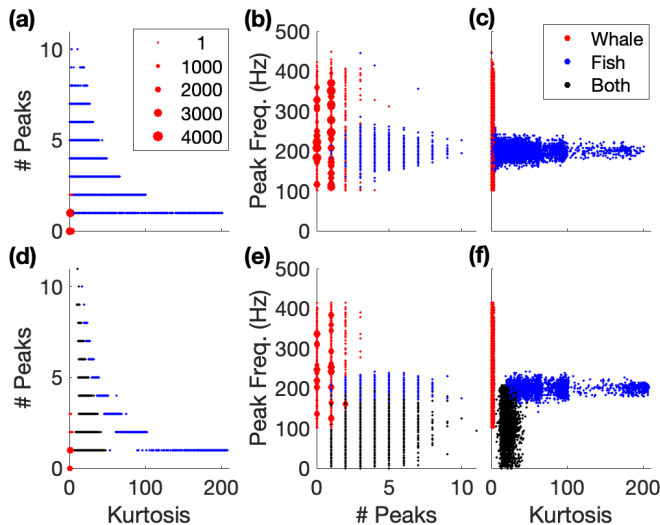


FIG. 9. Handpicked features demonstrate some separability by kurtosis, number of timeseries peaks, and peak frequency but with overlapping clusters for (a-c) two classes (whale, fish) and (d-f) (bottom) three classes (whale, fish, both). The dots are scaled to indicate density of feature pairs, with each dot increased by 1 pt for every 100 samples.

TABLE IV. Classification accuracy, precision, and recall on simulations for unsupervised clustering with hand-crafted features (K-means, hierarchical clustering) vs deep learning (DEC). Whale song was defined as the positive class.

Method	Accuracy	Recall	Precision
$K=2$			
K-means	0.73	0.47	0.99
Hierarchical	0.66	0.32	1.0
DEC ($P=10$)	0.99	0.99	0.99
$K=2$ (imbalanced)			
K-means	0.86	0.46	0.98
Hierarchical	0.87	0.50	0.97
DEC ($P=10$)	0.75	0.99	0.50
$K=3$			
K-means	0.77	0.49	1.0
Hierarchical	0.71	0.45	1.0
DEC ($P=15$)	0.86	0.99	0.96

Model parameters cannot be determined by cross-validation in unsupervised clustering due to its inherently label-free nature.[44] To achieve reasonable classification accuracy, a previously successful model architecture was employed,[37] and the simulation accuracy was examined for DEC with $K=2$ and $K=3$ equal-sized classes at varying latent feature vector dimensionality (Fig. 10). When the latent dimension was low, eg $P < 8$, all features were clustered in a single class. For 2 classes, accuracy was consistent when $P > 8$. For 3 classes, accuracy was unstable. The instability was likely caused by weak convergence and sensitivity to the weight initialization, but the minimum latent dimension was consistent across ran-

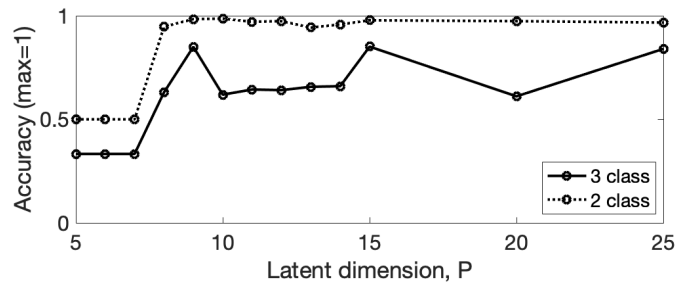


FIG. 10. Accuracy of DEC for 10000 simulated signals with varying latent dimension (P). $K=3$ classes contained fish, whale, or fish and whale, and $K=2$ classes had fish or whale. In both cases, the method fails at low P .

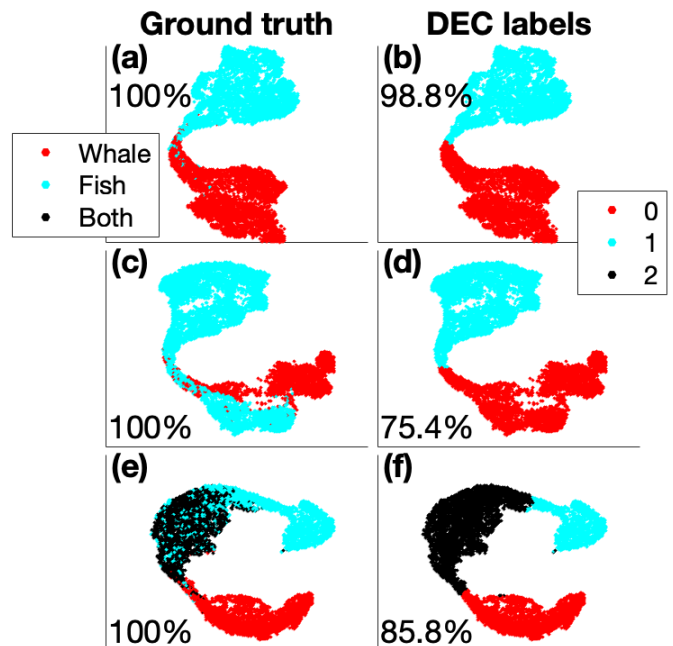


FIG. 11. t-SNE representation of the deep embedded feature vectors for 10000 simulated examples with (a,b) fish call and whale song classes, and (c,d) fish call, whale song, and fish/whale classes. The plots are colored by (a,c) ground truth labels and (b,d) DEC predicted labels. The perplexity value was 200.

dom seeds. In general, higher accuracy was achieved with higher latent dimension when $K=3$.

DEC clustering for 2 equal-sized classes is shown in Fig. 11(a,b) using a t-SNE representation of the $P=10$ -dimensional latent feature vector with perplexity 200. The high perplexity improved visualization, likely due to the large number of samples relative to the feature dimension. The point colors represent the two class labels. Signals that were spectrally similar were most likely to be misclassified, such as low-frequency FM sweeps and closely spaced fish pulse sequences lasting from 0.2 s to 0.4 s. In most cases, DEC successfully separated fish calls

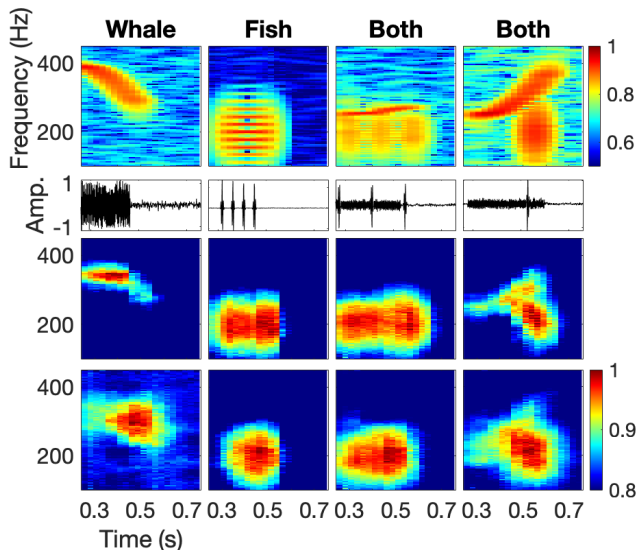


FIG. 12. Simulated coral reef bioacoustic signals successfully classified using DEC. From top to bottom rows: input spectrograms, simulated timeseries, initial DEC reconstruction, and DEC reconstruction after adding clustering loss.

and whale song into separate classes, with high accuracy, precision, and recall (Table IV).

For 2 imbalanced classes (2500 whale/7500 fish calls), DEC had reduced accuracy likely due to its convergence to equal-sized clusters as shown in Fig. 11(c,d). The reduction in precision and accuracy was directly proportional to the reduction in the class sizes (Table IV), while recall was unchanged because the whale song class was overestimated (Fig. 11(c,d)).

The addition of a combined signal class, using $K = 3$ equal-sized classes, demonstrated that overlapping signals were difficult to differentiate in the spectral domain (Fig. 11(e,f)). Most whale song events were correctly classified, as indicated by a high recall value. The largest classification overlap was between fish calls and combined class. Figure 12 shows that fish calls with large bandwidth and duration may dominate the spectral signature, which may lead to increased misclassification.

C. Experiment

The clustering methods from Sec. IV were applied to a subset of 10,000 unlabeled detections randomly selected from the Hawaii 2020 experiment. Each detection contained one or more directional signals with unknown SNR. Then, labels of whale song/no whale song (fish calls only) were manually assigned for 4000 samples or 40%, based on the signal within the detection window. About two-thirds were labeled as no whale song and contained only fish calls.

The results of clustering the $P = 6$ -dimensional hand-picked feature vectors with K-means and $K = 2$ are shown

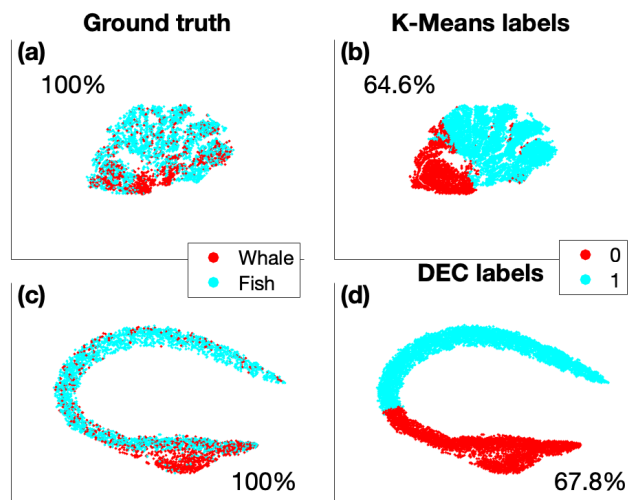


FIG. 13. Experimental data from a Hawaiian coral reef shown as a t-SNE representation of (a, b) $P = 6$ handpicked features and (c, d) DEC learned features for 10,000 random detections, colored by (a, c) hand-labeled classes and (b, d) K-means clustering with $K = 2$. The perplexity was 200 for DEC and 300 for the physical features.

TABLE V. Classification accuracy determined from manually labeled experimental detections for unsupervised clustering with handpicked features (K-means, hierarchical clustering) vs deep learning (DEC).

Method	Accuracy	Recall	Precision
K-means ($K = 2$)	0.65	0.41	0.44
Hierarchical ($K = 2$)	0.51	0.56	0.34
DEC ($P = 10, K = 2$)	0.68	0.83	0.60

using t-SNE in Fig. 13b. The overall accuracy, precision, and recall were low (Table V), indicating that the clustering methods did not align with the manual labels. Similar results were found for hierarchical clustering. These results were in line with the simulation results but suggest that feature extraction was less reliable in the experimental data.

Figure 13d shows the result of DEC with $P = 15$ using the normalized input spectrogram estimated from the detected signals. The DEC was pretrained for 5000 epochs in order to account for increased variability in the experimental data before updating clusters for 20 epochs. DEC accuracy was slightly higher than handpicked feature clustering, but the significantly higher recall value demonstrates that DEC correctly classified many of the whale song events. The class imbalance between whale song and fish calls, evident in Fig. 13c, was not well captured by the DEC algorithm used in this study, which converged towards well-balanced classes. The reduced accuracy and precision were a result of this imbalance.

Successfully classified spectrogram reconstructions and

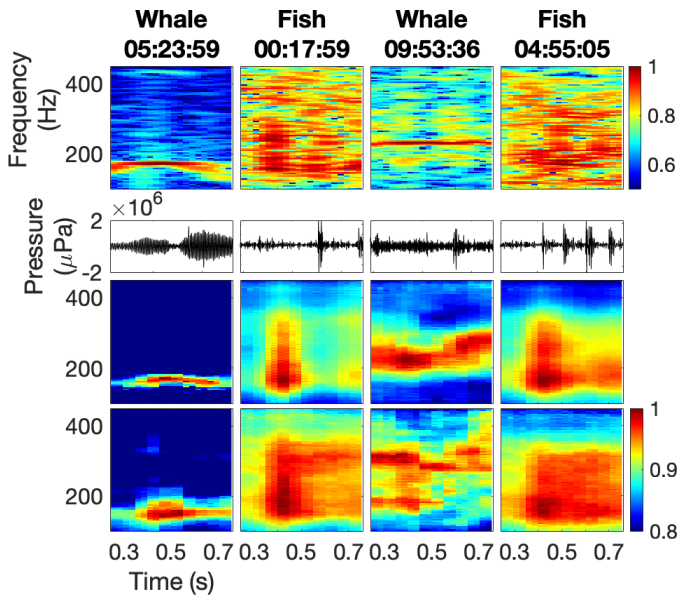


FIG. 14. Experimentally detected coral reef bioacoustic signals successfully classified using DEC. From top to bottom rows: input spectrograms, simulated timeseries, initial DEC reconstruction, and DEC reconstruction after adding clustering loss. The start time of each detection on February 25, 2020 is formatted as HH:MM:SS relative to midnight.

their corresponding timeseries are shown in Fig. 14. These demonstrate that whale song was primarily identified by its narrow bandwidth and temporal extent, whereas fish call pulse sequences were identified as broadband. The unscaled timeseries in Fig. 14 demonstrate the magnitude variation between events that was not attributed to signal type, motivating the normalization of the spectrograms.

VII. DISCUSSION

An unsupervised machine learning approach was presented for interpreting unlabeled coral reef bioacoustic detections. This approach considers and expands upon methods from recently proposed automatic fish call classifiers.[17, 22, 24]

Given the complex nature of the coral reef soundscape, two approaches were proposed to separate whale song from fish calls. First, handpicked features known to be correlated with coral reef fish species[25, 29, 42] and other relevant acoustic metrics[24, 28] were extracted. These features were clustered using hierarchical clustering and K-means. Then, the deep clustering approach DEC was used to jointly learn features and cluster labels directly from the spectrograms.

Clustering of simulated fish calls (Gaussian pulses) and whale song units (FM sweeps) demonstrated that handpicked features overlapped enough to reduce unsupervised clustering accuracy. By jointly learning features and clusters, DEC was successful in separating fish

calls and whale song directly from spectrograms. However, the DEC algorithm[13, 44] with parameters implemented in this study was observed to converge to equal-sized classes, resulting in higher misclassifications. A combined class with overlapping whale song and fish call also reduced DEC performance due to its inability to distinguish separate signals within the spectrograms. Handpicked feature clustering performed similarly with or without the inclusion of a combined class and demonstrated improved accuracy on imbalanced classes, indicating that the handpicked features were not evenly distributed in feature space. In all scenarios except the simulated imbalanced case, DEC had higher accuracy and recall than the handpicked clustering and was more likely to correctly classify existing whale song events.

A directional detector was used to identify potentially localizable broadband bioacoustic events on a Hawaiian coral reef in February–March 2020. A labeled subset of these detections with whale song/no whale song indicated that about two-thirds of the detections contained primarily fish calls and one-third contained a whale song segment.

Unsupervised K-means clustering of handpicked features with $K=2$ on the experimental, manually labeled data achieved low accuracy, precision, and recall. DEC with $K=2$ achieved similar accuracy, but its higher recall demonstrated its ability to correctly classify many whale song events. A class imbalance between whale song and fish calls likely led the DEC algorithm to define incorrect class boundaries (Fig. 13c,d), as evidenced in its lower precision. DEC reconstructions of the input spectrograms demonstrate that the learned features are representative of spectral features identified by manual labelers.

These results demonstrate that DEC is a promising method for clustering unlabeled bioacoustic signals with distinct spectral signatures. Our results indicate that the feature extraction process is key for unsupervised clustering of hand-picked features and that the feature distributions may be as or more important than their physical relations to the signal. Finally, class imbalance is an important consideration, particularly for unlabeled data where the class priors are unknown. As class imbalance is a common occurrence in ambient noise acoustics and geophysics, DEC clustering algorithms should be considered that jointly learn or regularize the weighted class priors as well as the cluster distributions.

VIII. ACKNOWLEDGEMENTS

Thank you to Greeneridge Sciences for providing the DASAR sensors and to Alex Conrad for assisting with DASAR post-processing. Thank you to Richard Walsh for assistance with hardware deployment and recovery. This work was supported by the Office of Naval research under award N00014-18-1-2065.

- [1] M. C. P. Amorim. Diversity of sound production in fish. *Commun. Fish*, 1:71–104, 2006.
- [2] P. C. Bermant, M. M. Bronstein, R. J. Wood, S. Gero, and D. F. Gruber. Deep machine learning techniques for the detection and classification of sperm whale bioacoustics. *Scientific Reports*, 9(1):12588, 2019.
- [3] M. J. Bianco, P. Gerstoft, J. Traer, E. Ozanich, M. A. Roch, S. Gannot, and C.-A. Deledalle. Machine learning in acoustics: Theory and applications. *J. Acoust. Soc. Am.*, 146(5):3590–3628, November 2019.
- [4] C. Biemann. *Structure Discovery in Natural Language: Theory and Applications of Natural Language Processing*, pages 73–75. Springer-Verlag, Berlin Heidelberg, 2012.
- [5] C. Bishop. *Pattern Recognition and Machine Learning*, volume 1, pages 424–428. Springer, New York, 2006.
- [6] F. Chollet, and Others Keras. <https://keras.io>, 2015.
- [7] Volker B Deecke and Vincent M Janik. Automated categorization of bioacoustic signals: avoiding perceptual pitfalls. *J. Acoust. Soc. Am.*, 119(1):645–653, 2006.
- [8] Esri. *National Geographic Style Map [basemap]*, November 23, 2020. <https://www.arcgis.com/home/webmap/>.
- [9] M. Abadi, A. Agarwal, P. Barham, E. Brevdo, Z. Chen, C. Citro, G. S. Corrado, A. Davis, J. Dean, M. Devin, S. Ghemawat, I. Goodfellow, A. Harp, G. Irving, M. Isard, Y. Jia, R. Jozefowicz, L. Kaiser, M. Kudlur, J. Levenberg, D. Mané, R. Monga, S. Moore, D. Murray, C. Olah, M. Schuster, J. Shlens, B. Steiner, I. Sutskever, K. Talwar, P. Tucker, V. Vanhoucke, V. Vasudevan, F. Viégas, O. Vinyals, P. Warden, M. Wattenberg, M. Wicke, Y. Yu, and X. Zheng. TensorFlow: Large-scale machine learning on heterogeneous systems, 2015. Software available from tensorflow.org.
- [10] K. E. Frasier, M. A. Roch, M. S. Soldevilla, S. M. Wiggins, L. P. Garrison, and J. A. Hildebrand. Automated classification of dolphin echolocation click types from the Gulf of Mexico. *PLOS Computational Biology*, 13(12):1–23, 12 2017.
- [11] Kaitlin E Frasier, E Elizabeth Henderson, Hannah R Bassett, and Marie A Roch. Automated identification and clustering of subunits within delphinid vocalizations. *Marine Mammal Sci.*, 32(3):911–930, 2016.
- [12] I. Goodfellow, Y. Bengio, and A. Courville. *Deep Learning*, chapter 14, pages 163–215, 493–495, 499–500. Massachusetts Institute of Technology, 2016.
- [13] X. Guo, L. Gao, X. Lui, and J. Yin. Improved deep embedded clustering with local structure preservation. *Proc. 26th Int. Joint Conf. Art. Intel. (IJCAI)*, pages 1753–1759, 2017.
- [14] L. V. D. Haaten and G. Hinton. J. mach. learn. res. *Visualizing data using t-SNE*, pages 2579–2605, 2008.
- [15] X. C. Halkias, S. Paris, and H. Glotin. Classification of mysticete sounds using machine learning techniques. *J. Acoust. Soc. Am.*, 134(5):3496–3505, 2013.
- [16] T. Hastie, R. Tibshirani, and J. Friedman. *Elements of Statistical Learning*, chapter 13.2.1, page 460. Springer, New York, second edition, 2009.
- [17] A. K. Ibrahim, H. Zhuang, L. M. Chérubin, M. T. Schärer-Umpierre, and N. Erdol. Automatic classification of grouper species by their sounds using deep neural networks. *J. Acoust. Soc. Am.*, 144(3):EL196–EL202, September 2018.
- [18] Jr. J. H. Ward. Hierarchical grouping to optimize an objective function. *Am. Stat. Ass. J.*, pages 236–244, March 1963.
- [19] D. P. Kingma and J. Ba. Adam: A Method for Stochastic Optimization. *Proc. of the 3rd ICLR*, 2014.
- [20] W. Lee and V. Staneva. Compact representation of temporal processes in echosounder time series via matrix decomposition, 2020.
- [21] R. V. Lenth. On Finding the Source of a Signal. *Technometrics*, 23(2):149–154, May 1981.
- [22] T.-H. Lin, Y. Tsao, and T. Akamatsu. Comparison of passive acoustic soniferous fish monitoring with supervised and unsupervised approaches. *J. Acoust. Soc. Am.*, 143(4):EL278–EL284, April 2018.
- [23] L. V. D. Maaten. Barnes-Hut-SNE. *CoRR*, abs/1301.3342, 2013.
- [24] M. Malfante, J. I. Mars, M. D. Mura, and C. Gervaise. Automatic fish sounds classification. *J. Acoust. Soc. Am.*, 143(5):2834–2846, May 2018.
- [25] D. A. Mann and P. S. Lobel. Propagation of damselfish (*Pomacentridae*) courtship sounds. *J. Acoust. Soc. Am.*, 101(6):3783–3791, February 1997.
- [26] S. Mann and S. Haykin. The Chirplet Transform: A Generalization of Gabor’s Logon Ttransform. *Vision Interface 1991*, pages 205–212, 1991.
- [27] D. Manolakis and J. G. Proakis. In *Digital Signal Processing: Principles, Algorithms, and Applications*, chapter 2.1.2, pages 47–52. Prentice-Hall International, Inc., 3rd edition, 1996.
- [28] S. B. Martin, K. Lucke, and D. R. Barclay. Techniques for distinguishing between impulsive and non-impulsive sound in the context of regulating sound exposure for marine mammals. *J. Acoust. Soc. Am.*, 147(4):2159–2176, April 2020.
- [29] K. P. Maruska, K. S. Boyle, L. R. Dewan, and T. C. Tricas. Sound production and spectral hearing sensitivity in the Hawaiian sergeant damselfish, *abundefduf abdominalis*. *J. Exp. Biol.*, 210:3990–4004, 2007.
- [30] Mathworks. Statistics and Machine Learning Toolbox: User’s Guide (R2019b), 2019. Access online 28 February 2020 at https://www.mathworks.com/help/pdf_doc/stats/stats.pdf.
- [31] B. McCowan. A new quantitative technique for categorizing whistles using simulated signal and whistles from captive bottlenose dolphins (*delphinidae, tursiops truncatus*). *Ethology*, 100(3):177–193, 1995.
- [32] D. K. Mellinger and C. W. Clark. Methods for automatic detection of mysticete sounds. *Marine Freshw. Behav. Phys.*, 29(1-4):163–181, 1997.
- [33] K. P. Murphy. *Machine Learning: A Probabilistic Perspective*, pages 389–397, 897–900. Massachusetts Institute of Technology, 2012.
- [34] M. A. Roch, H. Klinck, S. Baumann-Pickering, D. K. Mellinger, S. Qui, M. S. Soldevilla, and J. A. Hildebrand. Classification of echolocation clicks from odontocetes in the southern california bight. *The Journal of the Acoustical Society of America*, 129(1):467–475, 2011.
- [35] Y. Shiu, K. J. Palmer, M. Roch, E. Fleishman, X. Liu, E.-M. Nosal, T. Helble, D. Cholewiak, D. Gillespie, and H. Klinck. Deep neural networks for automated detection of marine mammal species. *Scientific Reports*, 10(1):607,

- 2020.
- [36] Evgeny Smirnov. North atlantic right whale call detection with convolutional neural networks. In *Int. Conf. on Mach. Learn.*, pages 78–79. Citeseer, 2013.
- [37] D. Snover, C. W. Johnson, M. J. Bianco, and P. Gerstoft. Deep Clustering to Identify Sources of Urban Seismic Noise in Long Beach, California. *Seismol. Res. Lett.*, pages 1–12, 2020.
- [38] W. W. Steiner. Species-specific differences in pure tonal whistle vocalizations of five western North Atlantic dolphin species. *Behav. Ecol. Sociobiol.*, 9(4):241–246, 1981.
- [39] D. Stowell and M. D. Plumbley. Automatic large-scale classification of bird sounds is strongly improved by unsupervised feature learning. *PeerJ*, 2:e488, 2014.
- [40] A. Thode, A.S. Conrad, R. Ozanich, E. King, S. E. Freeman, L. A. Freeman, B. Zgliczynski, P. Gerstoft, and K. H. Kim. Automated two-dimensional localization of underwater acoustic transient impulses using vector sensor image processing. *J. Acoust. Soc. Am.*, *In Review*.
- [41] A. M. Thode, K. H. Kim, R. G. Norman, S. B. Blackwell, and C. R. Greene. Acoustic vector sensor beamforming reduces masking from underwater industrial noise during passive monitoring. *J. Acoust. Soc. Am.*, 139(4):EL105–EL111, 2016.
- [42] T. C. Tricas and K. S. Boyle. Acoustic behaviors in Hawaiian coral reef fish communities. *Mar Ecol Prog Ser*, 511:1–16, September 2014.
- [43] P. Virtanen, R. Gommers, T. E. Oliphant, M. Haberland, T. Reddy, D. Cournapeau, E. Burovski, P. Peterson, W. Weckesser, J. Bright, S. J. van der Walt, M. Brett, J. Wilson, J. K. Millman, N. Mayorov, A. R. J. Nelson, E. Jones, R. Kern, E. Larson, C. J. Carey, A. Polat, Y. Feng, E. W. Moore, J. VanderPlas, D. Laxalde, J. Perktold, R. Cimrman, I. Henriksen, E. A. Quintero, C. R. Harris, A. M. Archibald, A. H. Ribeiro, F. Pedregosa, P. van Mulbregt, and SciPy 1.0 Contributors. SciPy 1.0: fundamental algorithms for scientific computing in Python. *Nature Methods*, 17(3):261–272, 2020.
- [44] J. Xie, R. Girshick, and A. Farhadi. Unsupervised deep embedded for clustering analysis. *Proc. 33rd Int. Conf. Mach. Learn.*, 2016.